Cement & Concrete Composites 33 (2011) 949–955

Contents lists available at ScienceDirect

Cement & Concrete Composites

journal homepage: www.elsevier.com/locate/cemconcomp

Simulation of rate dependent fracture in concrete using an irregular lattice model

Kunhwi Kim, Yun Mook Lim *

School of Civil & Environmental Engineering, College of Engineering, Yonsei University, Seoul 120-749, Republic of Korea

ARTICLE INFO

Article history:
Received 23 June 2010
Received in revised form 17 December 2010
Accepted 5 January 2011
Available online 8 January 2011

Keywords:
Dynamic fracture
Concrete
Rate dependency
Rigid-body-spring networks
Visco-plasticity

ABSTRACT

An irregular lattice model is used to simulate concrete fracture behavior under dynamic loadings. The numerical approach is based on rigid-body-spring networks, in which a visco-plastic damage model is applied to describe the rate dependency. A direct tensile test is simulated at various strain rates, and the dynamic strength increase is obtained in terms of dynamic increase factor (DIF). The DIFs are compared with a previous experimental and empirical study to calibrate the visco-plastic parameters. Next, a three-point-bending test is conducted numerically under impact and slow loadings, where the mixed-mode fracture is set up with a notch offset from the midspan. The rate-sensitive failure features are shown at the two different loading rates, and the rate effect on the failure mechanism is related with the peak load in the loading history. This study provides qualitative and quantitative understandings of the rate dependent failure behaviors in concrete.

1. Introduction

Concrete is a highly rate dependent material under dynamic loadings, which means that the macroscopic mechanical properties (e.g. strength, Young's modulus, fracture energy) depend on the loading rate. Moreover, such rate effects can lead to changes in the properties and failure modes of concrete structures [1,2]. Therefore, for simulating concrete structures subjected to dynamic loadings, material models should properly account for rate effects.

To establish and validate the material models, it is necessary to characterize their behaviors throughout the deformation stages and to quantify their responses under various loading states, in comparison with appropriate experimental results. The rate dependent behaviors of concrete have been investigated experimentally over a wide range of conditions. The range of strain rate examined is usually dictated by the particular type of loading devices employed. For instance, hydraulic testing machines are used to obtain strain rates up to about 1 s^{-1} [3,4] and the drop weight hammers are employed to impact specimens at strain rates on the order of 10 s^{-1} [5–8]. For strain rates on the order of 10–10^3 s^{-1}, the split Hopkinson pressure bar (SHPB) setup is employed and versatilely used to show the influence of high loading rates in tension and compression conditions [9–11]. Over the range of 10^2–10^4 s^{-1}, plate impact experiments have been carried out to achieve strain rates with the high hydrostatic pressure that exists in extremely dynamic conditions such as impact, penetration and blast [12].

As measured experimentally, strength generally increases with an increase in loading rate [10,13]. The strength increase is usually presented as a dynamic increase factor (DIF), which is the ratio of strengths measured under dynamic and quasi-static loading conditions, respectively. The DIFs from experimental results in tension and compression are shown in Fig. 1. These data illustrate that the rate effect is more pronounced in tension than in compression.

The rate dependency of concrete is thought to depend on two main factors: material inertia and moisture content within the micro- and nano-pores of the material [14]. However, these factors involve different physical mechanisms in separate ranges of strain rate. Material inertia mainly causes the strength increase at higher loading rates, whereas at intermediate loading rates moisture content is believed to play a dominant role in the rate dependency of concrete. Pedersen et al. [14] and Vegt et al. [15] have developed constitutive models that combine visco-elastic and visco-plastic elements to represent the two-mechanism rate dependency and simulated examples of concrete within the finite element (FE) framework. Nevertheless, continuum FE models rely on sophisticated techniques to obtain mesh-independent results for cracking and their applicability to modeling dynamic fracture is still in question.

From another point of view, the rate effects are assumed to be caused by dependence of the fracture process on the rate of crack opening and by the viscoelastic deformation of cement paste, aside from the inertia effects. The former dominates at higher strain rates and, even at moderate strain rates, material viscoelasticity would be insufficient to describe some other time-dependent effects, such as a reversal of softening into hardening after a

* Corresponding author. Tel.: +82 2 2123 2796; fax: +82 2 364 5300.
E-mail address: yunmook@yonsei.ac.kr (Y.M. Lim).

0958-9465/$ - see front matter © 2011 Elsevier Ltd. All rights reserved.
doi:10.1016/j.cemconcomp.2011.01.002

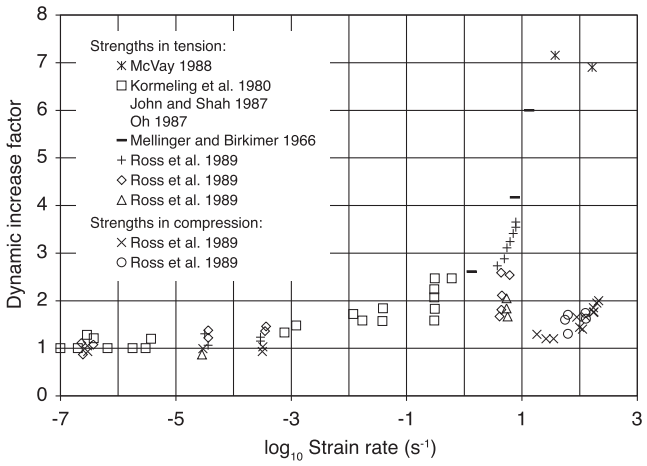

Fig. 1. The increase of dynamic strength over a wide range of strain rates. Note: References to the individual test programs are given by Ross et al. [10].

sudden increase of the loading rate [16]. This phenomenon can be reproduced by modeling rate dependence of fracture, in which fracture is regarded as a thermally activated process [17].

Discrete modeling approaches can be employed to analyze fracture behavior, and are complementary to continuum models. The distinct element method (DEM) [18] and molecular dynamics (MD) [19,20] have been adopted to perform fracture simulations in macro- and micro-scopic perspectives. Despite their capabilities for modeling dynamic fracture, the interactions of moving particles (with emphasis placed on the contact problem even before cracking) are not attractively used for practical fracture simulations. Cusatis et al. [17] have developed the lattice discrete particle model (LDPM) and used it to simulate concrete fracture for high loading rates of tension and compression. Yamamoto et al. [21] have confirmed the strength increase in rapid uniaxial and triaxial compression using a three dimensional rigid-body-spring model (RBSM). Those two models have achieved the rate effect by modifying the material properties as a function of loading rate. Recently, the peridynamic approach based on integral equations has been proposed to model displacement discontinuities (such as cracks) in materials without special mathematical techniques [22,23].

In this paper, the dynamic fracture behavior of concrete is simulated using the rigid-body-spring network (RBSN) framework, which has been developed for fracture simulations of concrete materials and structures under quasi-static loadings [24]. However, this meso-/macro-scopic model by itself does not adequately account for the rate effect caused by the aforementioned mechanisms in the concrete micro-structure, which contributes to strength gain at intermediate and higher strain rates. To resolve this problem, a visco-plastic damage model is implemented with nonlinear formulation of the constitutive relationship.

Numerical experiments are performed for the direct tensile test at various strain rate conditions. The strength increase is produced in terms of DIFs, which will be compared with the previous experimental data and an empirical formula [10] to calibrate the visco-plastic parameters of the constitutive equation. Next, a flexural test with a notched beam is simulated at two different loading rates to investigate the rate effect on failure patterns. The specimen is under three-point-bending configuration and a notch is offset from midspan to induce mixed-mode fracture [2]. The failure mode transition is observed in the specimen with different locations of the notch and the failure mechanism is associated with the loading response. The rate effect on the failure mechanism is also discussed.

2. Methodology

2.1. Modeling of concrete

The volume of concrete is modeled as an irregular assemblage of rigid particles interconnected with lattice elements (Fig. 2a) via random generation of nodal points [25] and the dual Delaunay–Voronoi tessellation [26]. A lattice element is defined within two neighboring particles of nodes i and j (Fig. 2b). The two nodes are connected via rigid-body constraints and a zero-size spring set (i.e., rigid-body-spring element) located at the center of the boundary segment. This spring set consists of two translational springs and one rotational spring in the local coordinates $(n-t-\phi)$ as depicted in Fig. 2b.

Element stiffness formulations are based on the discrete model concept of Kawai [27]. The element stiffness matrix is constructed by relating the element nodal displacement and the spring set local displacement, as described by Bolander and Saito [24]. The material matrix **D** has stiffness coefficients of the previously described springs in its diagonal entries (i.e., $\mathbf{D} = \mathrm{diag}[k_n, k_t, k_\phi]$). The Euclidean distance between the element nodes h and the length of the common boundary segment l are used to compute the stiffness coefficients

$$\begin{aligned} k_n &= \alpha_1 E t_e l/h, \\ k_t &= \alpha_2 k_n, \\ k_\phi &= k_n l^2/12, \end{aligned} \tag{1}$$

where t_e is the element thickness, and the factors α_1 and α_2 are adjustable parameters to represent Young's modulus E and Poisson ratio v. By adjusting α_1 and α_2, a global Poisson effect is achieved, but the point-wise Poisson representation within a local lattice is not reproduced properly. The restriction on the Poisson representation is a general concern to lattice models due to their unidirectional structures, and alternative approaches in Refs. [28,29] have been tried to remedy this problem yet particular limitations remain in use. In this study, the factors are set to unity (i.e., $\alpha_1 = \alpha_2 = 1$) where the lattice provides elastically homogeneous representation, although the corresponding $v = 0$. The approximation with zero Poisson ratio has been effective for simulating tensile fracture of concrete in the quasi-static regime [30], but, in dynamic regime, it needs to be considered carefully because the wave propagation exists and complicates the stress condition.

In dynamic analyses, the use of explicit time integration scheme requires considerations for the stability in the model. The system equation of motion has a lumped mass/inertia matrix in which the diagonal entries are calculated in proportion to the Voronoi polygon volume. Since the stiffness coefficients of each elements are irregular due to the random geometry of the Voronoi polygon, the estimation of the critical time increment for the stability condition is complicated. Thus, a simple relational expression of the critical time increment Δt_c is given by

$$\Delta t_c \propto \frac{d_m}{c}, \tag{2}$$

where d_m is a minimum allowable distance between nodes determined at the random generation of nodal points within the domain and $c = \sqrt{E/\rho}$ is the wave velocity, in which ρ is density. The distance d_m is associated with the lattice element length h (Fig. 2b), so the critical time increment is equivalent to the time required for a wave to traverse one element. Therefore, the model discretized with the smaller lattice scale demands to be analyzed in the smaller time increment for satisfying the stability condition like as in common FE simulations [31].

Concrete fracture is described by scaling the strengths and degrading the stiffnesses of the spring sets according to simple

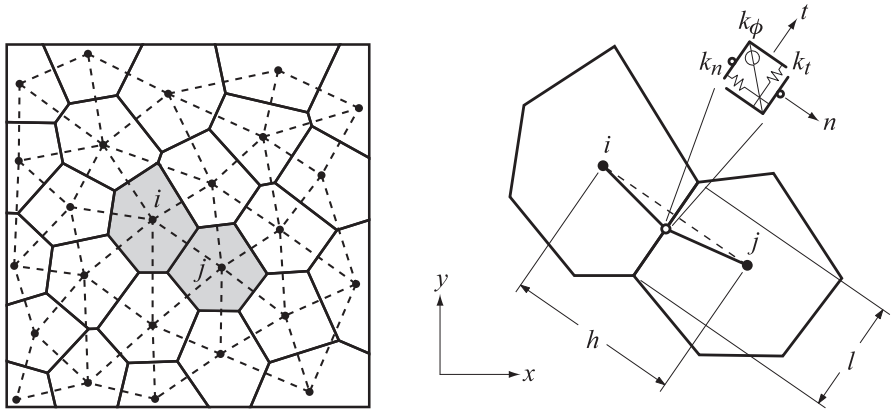

(a) domain discretization (b) lattice element between two particle nodes

Fig. 2. Rigid-body-spring network modeling of concrete.

breaking rules [32]. In a spring set, dividing the spring forces by the corresponding boundary segment area provides average stresses, s_n and s_t in the local coordinates. The stress components are each compared with separate fracture criteria. Cracking of the normal spring is taken into account by the effective uniaxial stress-strain relationship. Herein, the linear-softening diagram with $\epsilon_0 = 2G_F/f_t h$ is used for the post-peak behavior (Fig. 3a), where G_F is the fracture energy of each element. To represent fracture of the tangential spring, the Mohr–Coulomb surface is enacted as the stress limit, combined with a tension cut-off (Fig. 3b). If the vectorial stress pair (s_n, s_t) falls outside this limiting surface, the tangential stress is remapped onto the surface by degrading the tangential stiffness. Evolution of the limiting surface is guided by the stress–strain relationship of the normal spring. As shown in Fig. 3c, the rotational spring is elastic-perfectly plastic with the equivalent limiting moment

$$M_{eq} = \frac{t_e l^2}{6}\sigma_{nv}, \tag{3}$$

where σ_{nv} is the stress limit on of the normal spring.

2.2. Visco-plastic damage model

As mentioned above, concrete shows the rate dependency in which the physical mechanisms can be subdivided into two regimes: one associated with the material inertia and the other affected by moisture content. Material inertia dominates the rate effect at higher strain rates. The influence of rapid loading is transferred by means of the stress wave through the material, introducing the transient driving force to the crack propagation. Also, in the case of rapid crack propagation, material particles on the moving crack edges can bring about the inertial resistance to the advance of the crack [33]. At intermediate strain rates, the moisture content is assumed to exhibit the so-called Stefan effect [14]. The formation of capillaries in saturated pores within the cement paste causes a surface tension and the additional adhesion to resist the quick separation of the pores.

A rheological model with a visco-plastic contribution is developed to consider these rate dependent features. As depicted in Fig. 4, a spring has a connection with the visco-plastic components in series, for each degree of freedom in a spring set schematically. Note that the constitution of the schematic device is described in stress–strain relationship. The stiffness of the spring is evaluated by

$$\widehat{E} = (1-\omega)E, \tag{4}$$

where $0 \leqslant \omega \leqslant 1$ is a damage factor that increases with crack opening.

In the rheological model, total strain rate $\dot{\epsilon}$ is decomposed into an elastic strain rate $\dot{\epsilon}^e$ and a visco-plastic strain rate $\dot{\epsilon}^{vp}$ as

$$\dot{\epsilon} = \dot{\epsilon}^e + \dot{\epsilon}^{vp}, \tag{5}$$

and the stress σ is obtained as

$$\sigma = \widehat{E}\epsilon^e = \widehat{E}(\epsilon - \epsilon^{vp}). \tag{6}$$

The visco-plastic strain contribution is described according to the Perzyna type formulation [34]. For associative flow, the visco-plastic strain rate is expressed as

$$\dot{\epsilon}^{vp} = \frac{1}{\tau}\left[\frac{\langle f(\sigma)\rangle}{\widehat{E}}\right]^N \frac{\partial f(\sigma)}{\partial \sigma}, \qquad f(\sigma) := |\sigma| - \sigma_Y, \tag{7}$$

where τ is the effective relaxation time and N is the fitting parameter (a real number $N \geqslant 1$). These visco-plastic parameters will be calibrated in the next section. σ_Y is the maximum stress at yield conditions and $\langle f\rangle := (f + |f|)/2$ is denoted as the Macaulay function.

3. Direct tensile test

The simulation of direct tensile test is performed using the numerical model. The material specimen is discretized with 140 particles within dimensions of 100×50 mm as shown in Fig. 5. The loading conditions are defined at the particles of both left and right ends (10 particles at each side). The right end is moved laterally to the tensile direction by controlling the applied force $P(t)$ as a function of time, whereas the particles along the left end are fixed. The general strain rate can be configured according to the simple elastic relationship [35], here the strain rate is estimated as

$$\dot{\epsilon} = \frac{\dot{P}(t)}{E\sum A_e}, \tag{8}$$

where $\dot{P}(t)$ is the force rate applied on loaded particles and $\sum A_e$ is the sum of end-boundary segment area of the particles. The test is simulated in four cases of strain rates, 10^{-2}, 10^0, 10^1 and 10^2 s^{-1}.

The objective of the numerical experiment is to evaluate the dynamic strength increase and adjust the visco-plastic parameters in Eq. (7). The stress response is calculated for each time step by

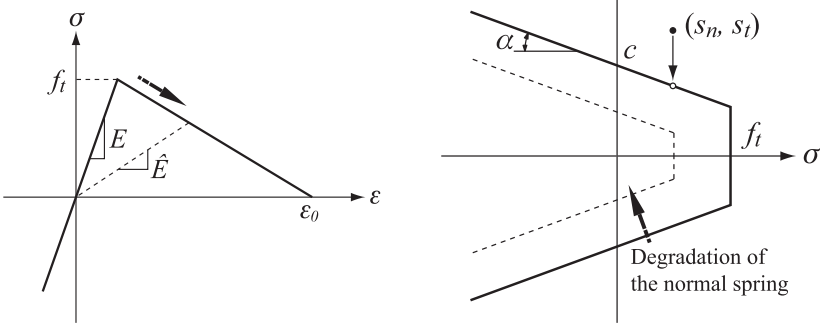

(a) effective uniaxial stress-strain relationship

(b) Mohr-Coulomb failure surface

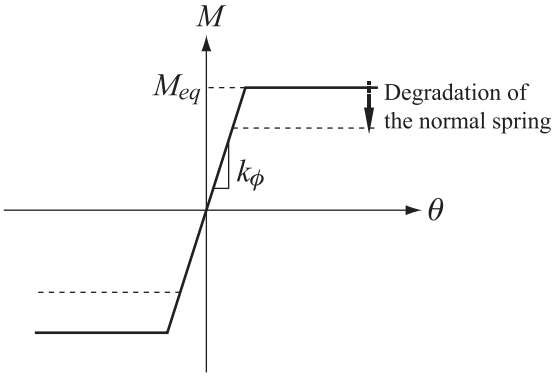

(c) effective moment-rotation relationship in perfect plasticity

Fig. 3. Fracture criteria of the rigid-body-spring elements.

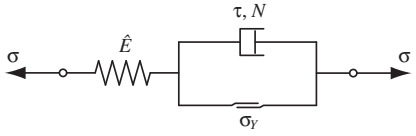

Fig. 4. Schematic rheological model of visco-plasticity.

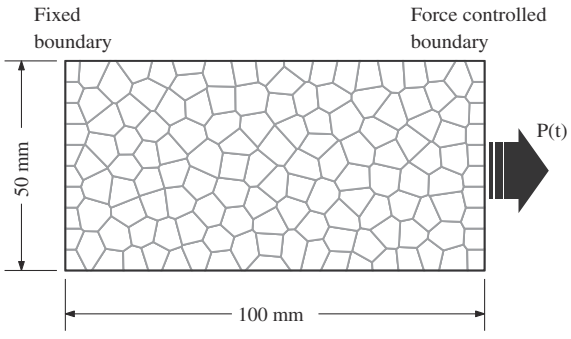

Fig. 5. Configuration of the direct tensile test specimen.

dividing the sum of reaction measured at the fixed particles by the sum of their end-boundary segment area. The tensile strength is evaluated as the peak value in the stress response time history to the tensile direction. The increase of tensile strength is represented by the DIF, the ratio of the measured peak stress to the static tensile strength. Fig. 6 shows the DIFs at the tested strain rates and the comparison of the values with the experimental data and the empirical formula obtained by Ross et al. [10]. They have arranged result sets from other previous experiments, which are also presented in the figure. Note that the strengths of materials (concrete and mortar) and the experimental methods (the direct tensile test and the splitting tensile test) are different in the referred experiments, but the DIFs have the similar distributions throughout the wide range of strain rates. Herein the material properties are as follows: static tensile strength $f_t = 2.06$ MPa, Young's modulus $E = 21.3$ GPa, density $\rho = 2018$ kg/m^3, adopted from [18]; and fracture energy $G_F = 24.03$ N/m, which is derived from an assumed maximum traction-free crack opening in the linear-softening diagram. By trial and error for fitting the DIFs from the numerical experiment, the set of the visco-plastic parameters that yields the best agreement with the experimental results is calibrated: $\tau = 5.5 \times 10^{-7}$ s and $N = 1.5$.

The DIFs from simulations without the visco-plastic damage model show slight increase up to about 1.17 at strain rate of 10^2 s^{-1}, as plotted in Fig. 6. It can be interpreted that the calculation with particle mass/inertia gives a negligible effect to reproduce the strength increase. Thus, the rate effect can be mainly presented by the visco-plastic damage model with the specific constitutive relationship in this meso-/macro-scopic numerical model.

In addition, to check the dependency of spatial discretization, the specimens modeled with the same lattice size (146 particles) and the refined lattices (880 particles and 3420 particles) are simulated under the exact same conditions. The DIFs are arranged in Table 1 with the empirical values from Ref. [10]. The results imply

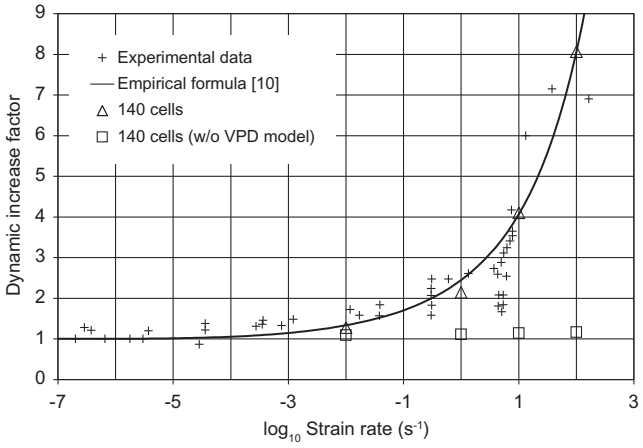

Fig. 6. Dynamic increase factor of tensile strength.

a slight difference depending on the discretization scale. In particular comparison of the same lattice size (between the specimens of 140 and 146 particles), the variability of the results is less than other cases of the finer lattices, which is due to the random nature of the lattice realization. On the temporal aspect, finely discretized model must be analyzed with small time increment as previously noted in Section 2.1.

4. Flexural beam test in mixed-mode fracture

The rate effect on the failure modes is analyzed through the simulation of flexural test with a notched beam. The test program proposed by John and Shah [2] is adapted for generic configuration of this simulation. As shown in Fig. 7, the beam is under three-point-bending condition and the degree of mixed-mode fracture is adjusted with location of the notch. The notch is offset from the midspan and its location is defined by the parameter γ; the value of $\gamma = 0$ corresponds to the mode I fracture configuration and if $\gamma = 1$, the specimen is unnotched.

Depending on the value of $0 < \gamma < 1$, two modes of failure are possible, as indicated by points 1 and 2 in Fig. 8 [36]. When $\gamma < \gamma_t$, mixed-mode failure occurs at the notch tip (Fig. 8a), whereas when $\gamma > \gamma_t$, flexural failure occurs at midspan (Fig. 8b). The case of $\gamma = \gamma_t$ defines the transition stage, in which failure can occur at both the notch and midspan (Fig. 8c). The objective of this simulation is to detect the transition stage as the notch is placed from the midspan to the end support. Seven test cases are simulated for $\gamma = 0.0$, 0.5, 0.6, 0.65, 0.7, 0.75 and 0.80.

To assess the rate dependency of the failure mode transition, two loading rates are considered: $\dot{\epsilon}_b = 0.01$ (slow rate) and 0.3 s^{-1} (impact rate), where $\dot{\epsilon}_b$ is the strain rate at the bottom of the midspan in the longitudinal direction. The loading condition is controlled by imposing a uniform velocity at the top, the value of which is related to $\dot{\epsilon}_b$. Allowing for the geometry of the beam

Table 1
Arrangement of dynamic increase factors by the discretization scale.

No. of particles	Dynamic increase factor at strain rate $\dot{\epsilon}$			
	10^{-2} s^{-1}	10^{0} s^{-1}	10^{1} s^{-1}	10^{2} s^{-1}
140	1.278	2.144	4.103	8.066
146	1.254	2.157	4.101	8.073
880	1.318	2.202	4.193	8.251
3420	1.334	2.219	4.211	8.286
Empirical	1.333	2.443	4.060	8.042

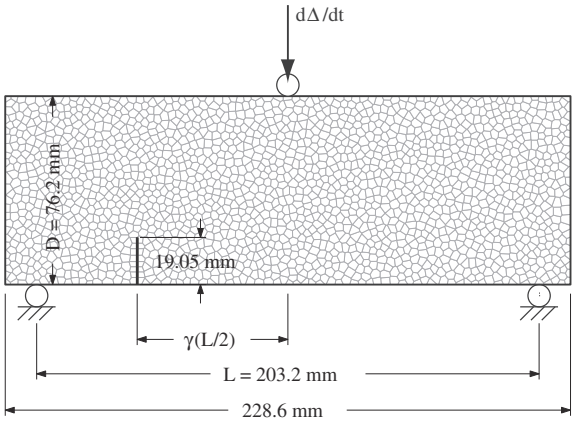

Fig. 7. Configuration of the notched-beam test specimen.

(Fig. 7), and neglecting the presence of any notch, the relationship between the two values is

$$\frac{d\Delta}{dt} = \frac{L^2}{6D}\dot{\epsilon}_b, \tag{9}$$

which is based on the elastic beam theory [37]. The material properties are obtained from the direct tensile test and the calibrated visco-plastic parameters are also applied to this test.

The failure deformations for all considered cases are arranged in Table 2, except the cases of $\gamma = 0.5$ and 0.8, where the crack patterns are analogous to the cases of $\gamma = 0.6$ and 0.75, respectively. The crack path is traced by the bold line on the cracked boundary segment and the displacement of each particle is multiplied by a factor of ten to increase visibility. As shown in the figure, the crack paths have tortuosity in the mixed-mode failure, which also has been observed in the experimental results [2]. This phenomenon may be provided due to the random lattice geometry in the model. For the case of $\gamma = 0.65$, at the slow rate, the specimen exhibits flexural failure at the midspan. At the impact loading rate, on the contrary, failure occurs from the notch tip in the specimen. The transition stage should lie between the value of $0.6 < \gamma_t < 0.65$ at the slow rate and $0.65 < \gamma_t < 0.70$ at the impact rate, respectively, though it is not detected explicitly. John and Shah [2] discuss these rate-sensitive features of failure and note that failure in a ductile manner (flexural failure) at the slow rate could become into the brittle failure behavior (diagonal tension-shear failure) at the impact rate. In this study, if we call the tendency to fracture at the notch tip in the mixed-mode *notch ascendency*, it can be interpreted that the notch ascendency is more pronounced as the strain rate increases.

The measured peak load for the two loading rates is plotted versus the location of the notch, γ, in Fig. 9. The chart indicates two trends: (1) the peak load value gradually increases in the region of γ up to 0.6 at the slow rate and 0.65 at the impact rate; and (2) in the region of greater γ, the peak load value exhibits a plateau. From observing the chart, the twofold failure mechanism is evident. Solid bullets indicate failure at the notch tip, with respect to the regime (1). Meanwhile, flexural failure at midspan is represented by hollow bullets, which relate to regime (2) where the beam fails as if the notch does not exist. Between these regimes, the transition stage should exist, in which the failure mechanism is switched. Here a discussion on the shift of the transition stage with the change of the loading rate can be given. Twofold failure mechanism yields two critical loads: one is calculated by assuming mixed-mode failure at the notch in the regime (1); and the second is calculated by assuming the flexural failure at the midspan within the regime (2). Between these two critical loads, the lower value is adopted to produce the peak load and the failure location. The increase of the

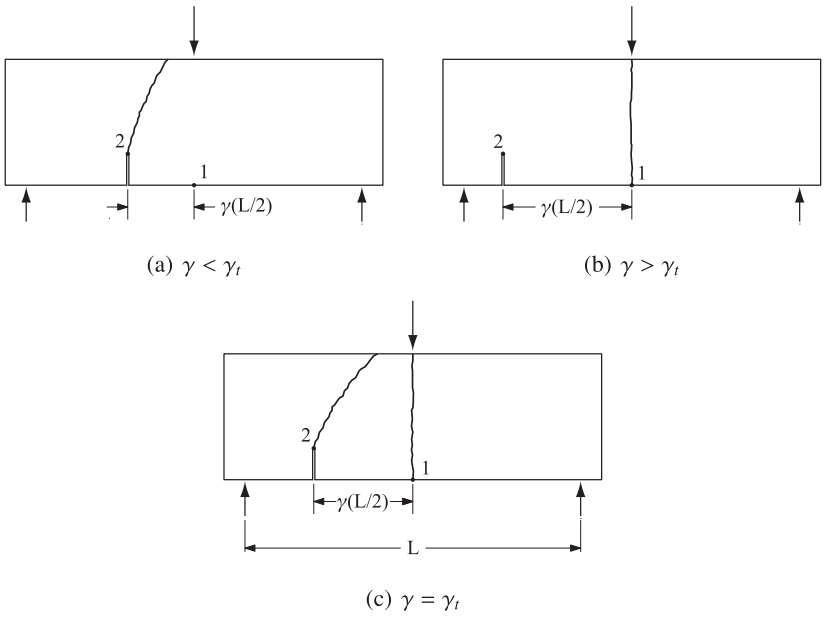

Fig. 8. Possible failure locations according to the location of the notch [36].

Table 2
Arrangement of final failure deformations and crack patterns.

	Slow rate ($\dot{\epsilon}_b$ =0.01 s^{-1})	Impact rate ($\dot{\epsilon}_b$ =0.3 s^{-1})
γ = 0.0	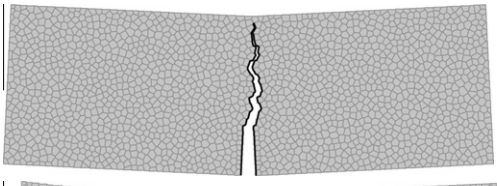	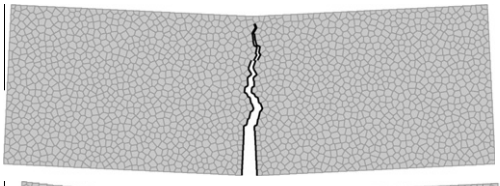
γ = 0.6	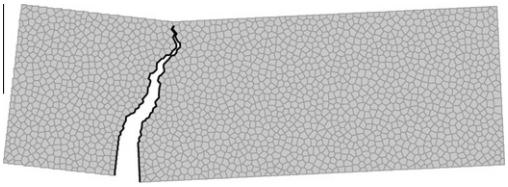	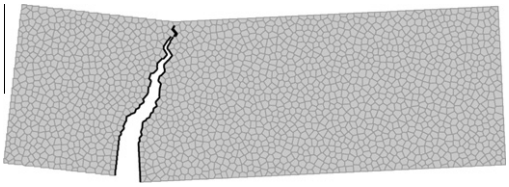
γ = 0.65	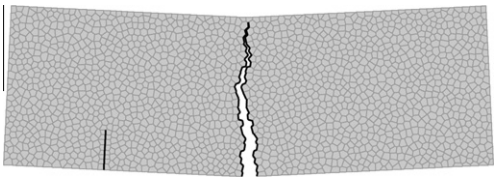	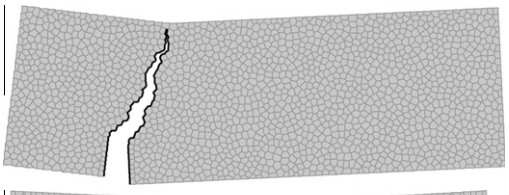
γ = 0.7	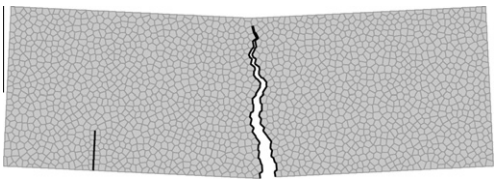	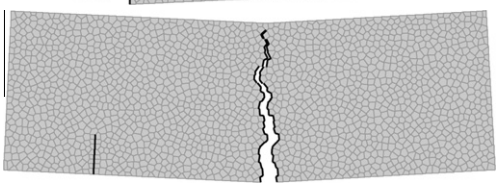
γ = 0.75	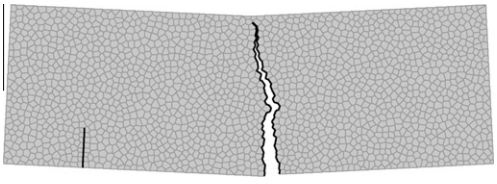	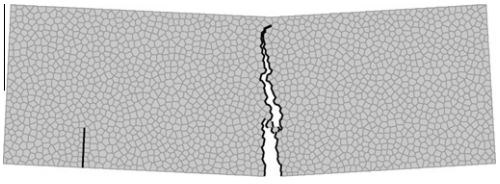

critical load associated with the mixed-mode failure at the impact rate is about 20% of average at the slow rate, whereas the flexural failure-induced critical load increases by 27% approximately. Thus, the difference in these increasing degrees is produced with the rate effect on the transition stage, which is also mentioned in the experimental and analytical results by John and Shah [2].

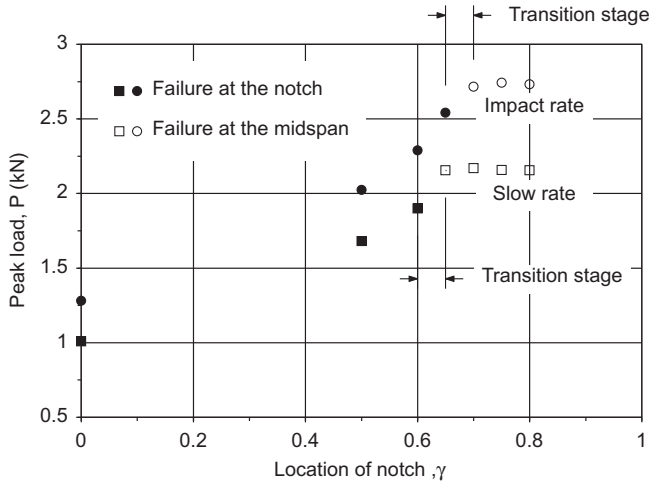

Fig. 9. Peak load corresponding to the location of the notch.

5. Summary and conclusions

This paper introduces an irregular lattice model with a visco-plastic damage scheme to simulate the rate dependency of concrete materials. The rate dependency of concrete is revealed not only through the change of material properties but also by the rate-sensitive failure modes in structures. This study shows the capabilities of the numerical model to reproduce the rate dependent fracture behavior in concrete. The results give qualitative and quantitative discussions of the rate dependency.

The direct tensile test is simulated with a simple rectangular specimen at various strain rates. The rate effect is reproduced by the mass/inertia of the lattice particle and the visco-plastic contribution of the model. The resulting strength increase is evaluated in terms of the DIF. By adjusting the visco-plastic parameters in the constitutive model, the value of the DIF falls in a good agreement with the experimental and the empirical results [10].

The simulation of the flexural beam test with mixed-mode fracture is performed at slow and impact loading rates and the fracture mode is controlled by the location of a notch. The failure mode transition is observed as the location of the notch is moved. As the loading rate increases, the transition stage in which both the mixed-mode failure and the flexural failure occur concurrently appears farther away from the midspan. The notch sensitivity, the tendency for failure to occur at a weak part such as a notch, should be considered in the dynamic fracture simulation of structures. Higher loading rate could lead to failure in a brittle manner, which is also considerable for structural dynamic response at intermediate loading rates, such as those caused by earthquakes [1]. The shift of the transition stage is also confirmed in the relationship between the peak load value and the location of the notch.

Acknowledgement

This research was supported by a grant from the LNG Plant R&D Center funded by the Ministry of Land, Transportation and Maritime Affairs(MLTM) of the Korean government.

References

[1] Shah SP, Wang ML, Chung L. Model concrete beam-column joints subjected to cyclic loading at two rates. Mater Struct 1987;20(2):85–95.
[2] John R, Shah SP. Mixed-mode fracture of concrete subjected to impact loading. J Struct Eng 1990;116(3):585–602.
[3] Takeda J, Tachikawa H. The mechanical properties of several kinds of concrete at compressive, tensile, and flexural tests in high rates of loading. Trans Archit Inst Jpn 1962;77:1–6.
[4] Bresler B, Bertero VV. Influence of high strain rate and cyclic loading of unconfined and confined concrete in compression. In: Proceedings of second Canadian conference on earthquake engineering, Hamilton, Ontario; 1975. p. 1–13.
[5] Watstein D. Effect of straining rate on the compressive strength and elastic properties of concrete. ACI J 1953;49(8):729–44.
[6] Hughes BP, Gregory R. Concrete subjected to high rates of loading in compression. Mag Concr Res 1972;24(78):25–36.
[7] Hughes BP, Watson AJ. Compressive strength and ultimate strain of concrete under impact loading. Mag Concr Res 1978;30(105):189–99.
[8] Zhu D, Gencoglu M, Mobasher B. Low velocity flexural impact behavior of AR glass fabric reinforced cement composites. Cem Concr Compos 2009;31(6):379–87.
[9] Reinhardt HW, Körmeling HA, Zielinski AJ. The split Hopkinson bar, a versatile tool for the impact testing of concrete. Mater Struct 1986;19(1):55–63.
[10] Ross CA, Thompson PY, Tedesco JW. Split-Hopkinson pressure-bar tests on concrete and mortar in tension and compression. ACI Mater J 1989;86(5):475–81.
[11] Yunsheng Z, Wei S, Sifeng L, Chujie J, Jianzhong L. Preparation of C200 green reactive powder concrete and its static–dynamic behaviors. Cem Concr Compos 2008;30(9):831–8.
[12] Grote DL, Park SW, Zhou M. Dynamic behavior of concrete at high strain rates and pressures: I. Experimental characterization. Int J Impact Eng 2001;25(9):869–86.
[13] Barpi F. Impact behaviour of concrete: a computational approach. Eng Fract Mech 2004;71(15):2197–213.
[14] Pedersen RR, Simone A, Sluys LJ. An analysis of dynamic fracture in concrete with a continuum visco-elastic visco-plastic damage model. Eng Fract Mech 2008;75(13):3782–805.
[15] Vegt I, Weerheijm J, Pedersen RR, Sluys LJ. Modelling of impact behaviour of concrete – an experimental approach. In: Meschke G, de Borst R, Mang H, Bićanić N, editors. Computational modelling of concrete structures – EURO-C 2006, Mayrhofen, Tyrol, Austria; 2006. p. 451–8.
[16] Bažant ZP, Gu WH, Faber KT. Softening reversal and other effects of a change in loading rate on fracture of concrete. ACI Mater J 1995;92(1):3–9.
[17] Cusatis G, Mencarelli A, Pelessone D, Baylot JT. Lattice discrete particle model (LDPM) for fracture dynamics and rate effect in concrete. In: Proceedings of the 2008 ASCE structures congress. Vancouver; 2008 [CD-ROM].
[18] Masuya H, Kajikawa Y, Nakata Y. Application of the distinct element method to the analysis of the concrete members under impact. Nucl Eng Des 1994;150(2-3):367–77.
[19] Wagner NJ, Holian BL, Voter AF. Molecular-dynamics simulations of two-dimensional materials at high strain rates. Phys Rev A 1992;45(12):8457–70.
[20] Kim K, Lim J, Kim J, Lim YM. Simulation of material failure behavior under different loading rates using molecular dynamics. Struct Eng Mech 2008;30(2):177–90.
[21] Yamamoto Y, Kuroda I, Furuya N. Dynamic fracture simulation of concrete in compression using 3D RBSM. In: Proceedings of second international workshop on performance, protection & strengthening of structures under extreme loading, Hayama, Japan; 2009 [CD-ROM].
[22] Silling SA. Reformulation of elasticity theory for discontinuities and long-range forces. J Mech Phys Solids 2000;48(1):175–209.
[23] Gerstle W, Sau N, Silling S. Peridynamic modeling of concrete structures. Nucl Eng Des 2007;237(12-13):1250–8.
[24] Bolander JE, Saito S. Fracture analyses using spring networks with random geometry. Eng Fract Mech 1998;61(5–6):569–91.
[25] Widom B. Random sequential addition of hard spheres to a volume. J Chem Phys 1966;44:3888–94.
[26] Preparata FP, Shamos MI. Computational geometry: an introduction. New York: Springer-Verlag; 1985.
[27] Kawai T. New discrete models and their application to seismic response analysis of structures. Nucl Eng Des 1978;48:207–29.
[28] Yip M, Mohle J, Bolander JE. Automated modeling of three-dimensional structural components using irregular lattices. Comput-Aided Civil Infrastruct Eng 2005;20(6):393–407.
[29] Cusatis G, Schauffert EA. Discontinuous cell method (DCM) for cohesive fracture propagation. In: Proceedings of 7th international conference on fracture mechanics of concrete and concrete structures (FraMCoS-7); 2010 [CD-ROM].
[30] Berton S, Bolander JE. Crack band model of fracture in irregular lattices. Comput Meth Appl Mech Eng 2006;195(52):7172–81.
[31] Hughes TJR. The finite element method: linear static and dynamic finite element analysis. New York: Dover Publications; 2000.
[32] Jagota A, Bennison SJ. Element breaking rules in computational models for brittle fracture. Modell Simul Mater Sci Eng 1995;3(4):485–501.
[33] Freund LB. Dynamic fracture mechanics. Cambridge University Press; 1998.
[34] Simo JC, Hughes TJR. Computational inelasticity. Springer; 2000.
[35] Siregar RA. Daimaruya M, Fuad K. Dynamic splitting-tensile test and numerical analysis for brittle materials. In: Proceedings of solid state science and technology, ICSSST 2006, vol. 909. AIP Conference Proceedings; 2007. p. 68–73.
[36] Jenq YS, Shah SP. Mixed-mode fracture of concrete. Int J Fract 1988;38(2):123–42.
[37] Ruiz G, Pandolfi A, Ortiz M. Three-dimensional cohesive modeling of dynamic mixed-mode fracture. Int J Numer Meth Eng 2001;52:97–120.